AIAA JOURNAL
Vol. 46, No. 6, June 2008

Nonlinear Flutter Calculations Using Finite Elements in a Direct Eulerian–Lagrangian Formulation

Guclu Seber* and Oddvar O. Bendiksen†
University of California, Los Angeles, Los Angeles, California 90095-1597

DOI: 10.2514/1.27844

A fully nonlinear aeroelastic formulation of the direct Eulerian–Lagrangian computational scheme is presented in which both structural and aerodynamic nonlinearities are treated without approximations. The method is direct in the sense that the calculations are done at the finite element level, both in the fluid and structural domains, and the fluid–structure system is time-marched as a single dynamic system using a multistage Runge–Kutta scheme. The exact nonlinear boundary condition at the fluid–structure boundary is satisfied based on the actual deformation of the wing. The generalized forces associated with the in-plane and out-of-plane degrees of freedom are calculated in local Lagrangian element coordinate systems that fully account for large rigid-body translations and rotations. Finite rotation relations are used to update the nodal deformation vectors at the end of each time step. Numerical results are presented for several nonlinear static and dynamic examples for which published results are available. Results of aeroelastic calculations using the new nonlinear model demonstrate the importance of including the nonlinear stiffening arising from the in-plane strains when calculating limit-cycle-oscillation amplitudes of wings of low-to-moderate aspect ratios and the limitations of the von Kármán nonlinear plate model in these cases.

Nomenclature

A_i	=	triangular area coordinates, $i = 1,2,3$
c_r	=	wing root chord
E	=	Young's modulus of elasticity
E_{tot}	=	total energy of the structure, $T + U$
e	=	total energy (fluid)
G	=	shear modulus of elasticity
h	=	plate thickness
k	=	shear correction factor
M	=	Mach number
$\boldsymbol{n}$	=	rotation vector
$\boldsymbol{n}_d$	=	deformed nodal vector
p	=	pressure
$\boldsymbol{q}$	=	generalized coordinate vector
T	=	kinetic energy
t	=	time
U	=	strain energy
$\boldsymbol{U}$	=	mesh velocity vector with components U_i
u, v, w	=	plate displacements in the x, y, and z directions
$\boldsymbol{u}$	=	fluid velocity vector with components $\boldsymbol{u}_i$
α	=	angle of attack
β_x, β_y	=	rotations of normals in the x–z and y–z planes, respectively
γ	=	ratio of specific heats
$\{\gamma\}$	=	shear strains
$\{\varepsilon_m\}$	=	membrane strains
$\{\varepsilon_n\}$	=	nonlinear strains
$\{\kappa\}$	=	plate element curvatures
Λ	=	sweep angle
λ	=	taper ratio
ν	=	Poisson's ratio
ρ	=	density
τ	=	nondimensional time, $\omega_{1T}t/2\pi$
ω	=	circular frequency
ω_{1T}	=	frequency of first torsion mode in vacuum

Superscripts

G	=	global (Eulerian) coordinate system
L	=	local (Lagrangian) coordinate system

Presented as Paper 1836 at the AIAA Structures, Structural Dynamics, and Materials Conference, Austin, TX, 18–21 April 2005; received 15 September 2006; revision received 25 November 2007; accepted for publication 6 December 2007.

*Ph.D. Candidate, Mechanical and Aerospace Engineering Department; currently Lecturer, Aerospace Engineering Department, Middle East Technical University, Ankara, Turkey. Member AIAA.

†Professor. Associate Fellow AIAA.

I. Introduction

ADVANCES in computational aeroelasticity over the past 25 years have made it possible to study a number of inherently nonlinear aeroelastic problems, such as transonic flutter of wings and panels, in which aerodynamic and/or structural nonlinearities result in limit-cycle flutter or limit-cycle oscillations (LCO) [1–9]. Until recently, most computational studies have emphasized the aerodynamic nonlinearities for two reasons. First, if a computational fluid dynamics (CFD)-based time-marching flutter calculation is necessary, the nonlinear version of the aerodynamic code represents the natural implementation, and no significant increase in speed or decrease in implementation complexity is achieved by linearizing the code. Second, the use of a linear structural model greatly simplifies the calculations, because the well-established modal methods from structural dynamics can still be used, either in a finite element (FE) or in a Rayleigh–Ritz setting.

Although linear structural models may yield reasonable results near the linear flutter boundary, they cannot be expected to give reliable results for the limit-cycle amplitudes at dynamic pressures significantly past the flutter boundary. In the transonic panel flutter problem, for example, the stiffening effect from the in-plane strains grows rapidly with increasing panel flutter amplitude, as calculated by the von Kármán theory, and the limit-cycle amplitude is reached very quickly [3]. In all the transonic cases studied in [3], no corresponding flutter solutions could be obtained using a linear structural model (nonphysical divergence occurred).

Many of the emerging problems in aeroelasticity involve very flexible structures, such as highly optimized unmanned aerial vehicles (UAVs) and high-altitude long-endurance (HALE)-type aircraft. The Helios aircraft built by AeroVironment and operated by NASA is a good example, in which wing tip deformations during steady flight were in the range of 10–20 ft, with dynamic excursions

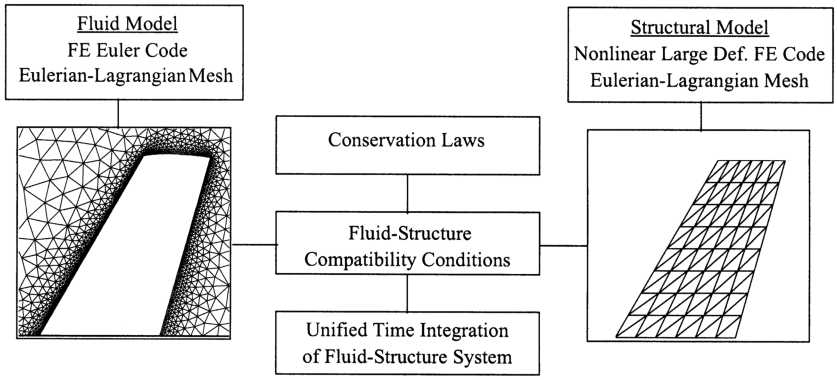

Fig. 1 The direct Eulerian–Lagrangian computational approach to fluid–structure interaction problems.

beyond 20 ft.[‡] Linear structural codes cannot be expected to give reliable aeroelastic results for these types of aircraft.

The von Kármán nonlinear plate model has been used in some recent studies of limit-cycle flutter of low-aspect-ratio wings [5,7], with mixed success. Our results indicate that it is a poor candidate for a general-purpose nonlinear aeroelastic code, because of its relatively limited range of validity and high sensitivity to the in-plane boundary conditions. For plates with all edges fixed or simply supported, as in a panel flutter calculation, for example, the von Kármán model performs reasonably well. But in the case of a cantilever low-aspect-ratio swept wing, it greatly overestimates the stiffening effect from in-plane strains, leading to a significant underestimation of the LCO amplitudes. This excess stiffness is clearly evident in experiment-theory comparisons of LCO amplitudes of flat-plate delta wings carried out in [5,7].

Furthermore, in a time-marching computational setting, the von Kármán plate model and similar 1-D beam models have a tendency to lock up and prevent convergence to the correct solution.

In this paper, a fully nonlinear formulation of the direct Eulerian–Lagrangian computational scheme [10] is presented, as shown in Fig. 1, in which both structural and aerodynamic nonlinearities are treated without approximations. The method is "direct" in the sense that the calculations are done at the finite element level, both in the fluid and structural domains, and the fluid–structure system is time-marched as a single dynamic system using a multistage Runge–Kutta scheme. Furthermore, the generalized forces associated with the in-plane and out-of-plane degrees of freedom are calculated in a local Lagrangian (element) coordinate system that fully accounts for large rigid-body translations and rotations. The exact nonlinear boundary condition at the fluid–structure boundary is satisfied using the *actual* deformation of the wing, as defined by the finite element shape functions and the local element coordinates. Although this type of implementation is more difficult than a loosely coupled scheme that lacks strict synchronization and is typically based on classical fluid–structure coupling at a "virtual surface" introduced for interpolation purposes, it is essential for obtaining the correct energy exchange between the fluid and the structure. This is an important numerical consideration in aeroelastic stability calculations.

II. Theoretical Formulation

A. Nonlinear Structural Model

In this study, the linear model previously used in [4,11] is modified to account for large deformations and to include additional degrees of freedom to model the in-plane motion of the wing. This model is based on a specific type of aeroelastic wing construction that has been used extensively in wind-tunnel tests. The structural part of the model is a thin, flat, aluminum-alloy plate of the same planform as the wing and covered by balsa wood or lightweight foam to form a smooth airfoil of the desired shape.

[‡]The Helios aircraft was destroyed in a flight mishap in June 2003. The instability that caused the structural breakup of the aircraft appears to have involved nonlinear aero–structural–control interactions.

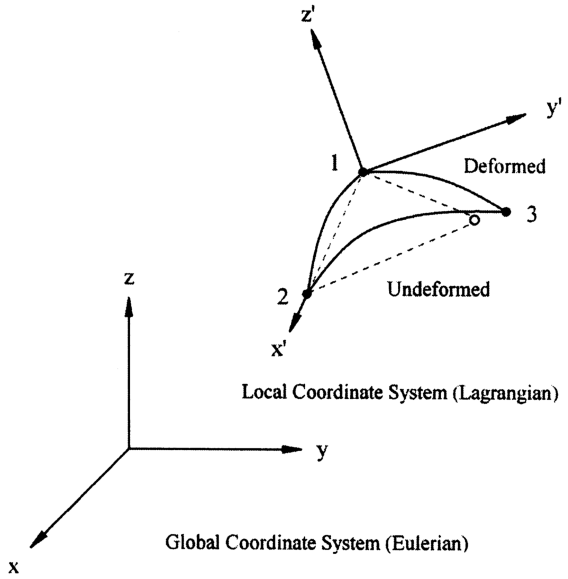

Fig. 2 Eulerian and Lagrangian coordinate systems.

The approach used in developing the new structural finite element model is best described as *mixed Eulerian–Lagrangian*, because it uses several element-attached Lagrangian coordinate systems to describe the arbitrarily large plate response with respect to a fixed Eulerian global system. Figure 2 shows a typical triangular structural finite element in its deformed configuration. The x–y–z coordinate system is the fixed Eulerian coordinate system with respect to which the response of the wing structure is expressed, and the x'–y'–z' system is an element-attached local coordinate system. It is Lagrangian in the sense that it moves with the corresponding element.

At any time step, the three nodes of a triangle form a plane in the global coordinate system. The z' axis can be defined with respect to this plane by taking the cross product of the two vectors defined by the triangle edges 1–2 and 1–3. The orientations of the x' and y' axes are arbitrary, and any convenient set may be chosen as long as it is consistent. In this study, the x' axis is aligned along nodes 1 and 2 of the triangular elements. Once the orientations of the z' and x' axes have been fixed, the remaining y' axis orientation is determined such that a right-handed coordinate system is formed. Any vector (displacements, forces, etc.) can be expressed in either the local element coordinates or the global system coordinates, and the two representations are related through the orthogonal transformation:

$$\boldsymbol{q}^L = [e]\boldsymbol{q}^G \tag{1}$$

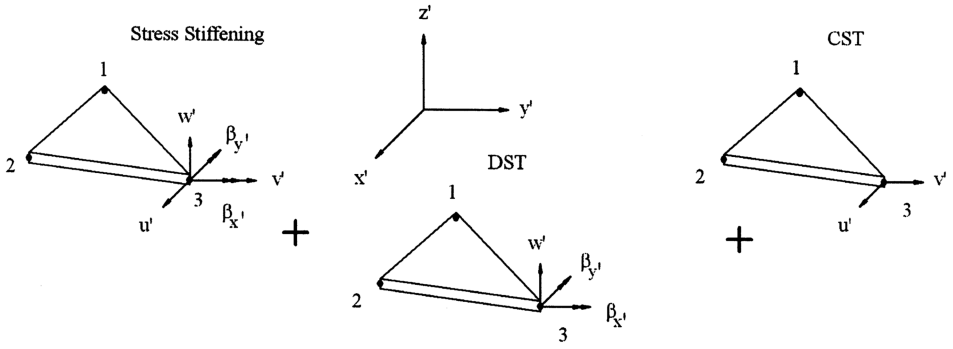

Fig. 3 Components of the nonlinear finite element.

$$[e] = \begin{bmatrix} (e_{x'})_1 & (e_{x'})_2 & (e_{x'})_3 \\ (e_{y'})_1 & (e_{y'})_2 & (e_{y'})_3 \\ (e_{z'})_1 & (e_{z'})_2 & (e_{z'})_3 \end{bmatrix} \tag{2}$$

In Eqs. (1) and (2), $\boldsymbol{q}^L$ and $\boldsymbol{q}^G$ are vectors expressed in the local and global coordinate systems, respectively, and $(e_{x'})_i$, $(e_{y'})_i$, and $(e_{z'})_i$ $(i = 1, 2, 3)$ are the components of the local coordinate system unit vectors expressed in the global coordinate system. They are also the direction cosines between the corresponding coordinate axes.

The nonlinear structural model employs three basic finite elements to model the in-plane, out-of-plane, and nonlinear behaviors, as shown in Fig. 3. First, a discrete shear triangle (DST) is used to model the out-of-plane bending and the transverse shear behavior. This element is based on the formulation in [12] and is extended to dynamics problems in [13]. It is free of shear locking, has the proper rank, and converges to the discrete Kirchhoff triangular element when the shear deformations become negligible. To obtain an element free of shear locking, the equilibrium equations are used to solve for the transverse shear strains, with the help of the constitutive equations.

Second, a constant strain triangle (CST) is used to model the in-plane behavior. The in-plane shape functions are used together with the corresponding shape functions of the DST to create the stress-stiffening matrix in local element coordinates.

Third, a stress-stiffening matrix provides the in-plane and out-of plane coupling effects. It is based on the von Kármán plate theory, which assumes that the nonlinear strain components arising from the in-plane displacement gradients are small compared with the corresponding terms arising from the transverse displacement gradients and may therefore be neglected. Although this results in an "incomplete set" of Green–Lagrange strains that cannot model arbitrary large deformations, it is not an issue here, because the deformations relative to the *local* Lagrangian element coordinate system are always small. It should be emphasized that the von Kármán theory would not result in a satisfactory stress-stiffening matrix with respect to the *global* coordinates (see the comparative results in Sec. III). To obtain unique and symmetric stress-stiffening matrices, we follow the derivations by Rajasekaran and Murray [14].

The total strain energy of an element can be expressed as a sum of the component strain energies, as follows:

$$U^e_{\text{total}} = U_m + U_b + U_s + U_{N1} + U_{N2} \tag{3}$$

$$U_m = \frac{1}{2}\int_A \lfloor \varepsilon_m \rfloor [D_m] \{\varepsilon_m\}\, dA \tag{4a}$$

$$U_b = \frac{1}{2}\int_A \lfloor \kappa \rfloor [D_b] \{\kappa\}\, dA \tag{4b}$$

$$U_s = \frac{1}{2}\int_A \lfloor \gamma \rfloor [D_s] \{\gamma\}\, dA \tag{4c}$$

$$U_{N1} = \int_A \lfloor \varepsilon_m \rfloor [D_m] \{\varepsilon_n\}\, dA \tag{4d}$$

$$U_{N2} = \int_A \lfloor \varepsilon_n \rfloor [D_m] \{\varepsilon_n\}\, dA \tag{4e}$$

where

$$[D] = \frac{E}{1-\nu^2}\begin{bmatrix} 1 & \nu & 0 \\ \nu & 1 & 0 \\ 0 & 0 & \frac{1-\nu}{2} \end{bmatrix} \tag{5a}$$

$$[D_m] = h[D], \qquad [D_b] = \frac{h^3}{12}[D] \tag{5b}$$

$$[D_s] = khG\begin{bmatrix} 1 & 0 \\ 0 & 1 \end{bmatrix} \tag{5c}$$

and k is the shear correction factor ($\frac{5}{6}$ for isotropic plates). In Eqs. (4), U_m, U_b, and U_s are the quadratic-order strain energies representing the membrane stretching (CST), out-of-plane bending, and shear (DST), respectively. The cubic-order strain energy U_{N1} [Eq. (4d)] represents the nonlinear coupling of the in-plane and out-of-plane motions, and the quartic-order strain energy U_{N2} [Eq. (4e)] represents the nonlinear coupling effect of slope due to large deflections. The strains and curvatures are related to the element displacements as follows:

$$\lfloor \varepsilon_m \rfloor = \left\{ \frac{\partial u'}{\partial x'} \quad \frac{\partial v'}{\partial y'} \quad \frac{\partial v'}{\partial x'} + \frac{\partial u'}{\partial y'} \right\} \tag{6a}$$

$$\lfloor \gamma \rfloor = \left\{ \frac{\partial w'}{\partial x'} + \beta_{x'} \quad \frac{\partial w'}{\partial y'} + \beta_{y'} \right\} \tag{6b}$$

$$\lfloor \varepsilon_n \rfloor = \left\{ \tfrac{1}{2}\beta^2_{x'} \quad \tfrac{1}{2}\beta^2_{y'} \quad \beta_{x'}\beta_{y'} \right\} \tag{6c}$$

$$\lfloor \kappa \rfloor = \left\{ \frac{\partial \beta_{x'}}{\partial x'} \quad \frac{\partial \beta_{y'}}{\partial y'} \quad \frac{\partial \beta_{x'}}{\partial y'} + \frac{\partial \beta_{y'}}{\partial x'} \right\} \tag{6d}$$

where

$$u' = u'_0(x', y', t) + z'\beta_{x'}(x', y', t) \tag{7a}$$

$$v' = v'_0(x', y', t) + z'\beta_{y'}(x', y', t) \tag{7b}$$

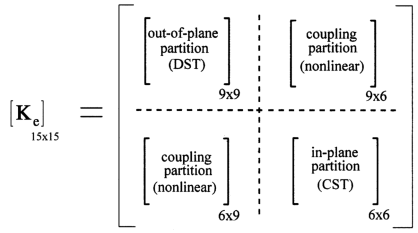

Fig. 4 Partitions of element stiffness matrix.

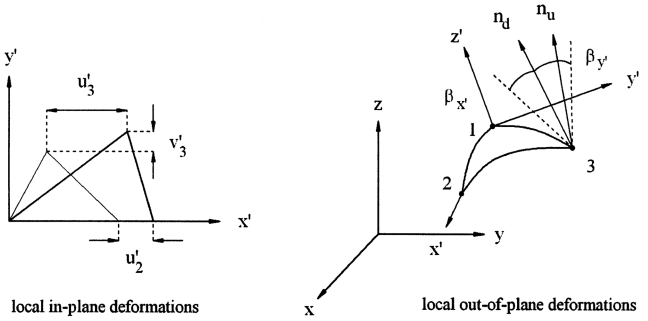

Fig. 5 Local in-plane and out-of-plane deformations.

$$w' = w'(x', y', t) \tag{7c}$$

are the displacement of the middle surface of the plate, and $\beta_{x'}$ and $\beta_{y'}$ are the rotation fields. The stiffness matrix for the DST element is based on quadratic interpolation of the rotation fields (see [12,15]). The stiffness matrix for the CST element is based on linear interpolation functions.

The complete element stiffness matrix of the nonlinear model can be obtained from the principle of stationary potential energy using the strain energy relations (4a–4e). To calculate the nonlinear coupling partition, the values of the nodal degrees of freedom are required at the current time step (discussed later). The structure of the element stiffness matrix is shown in Fig. 4.

By setting up the local coordinate systems using the triangle vertices as shown in Fig. 2, the number of nonzero nodal degrees of freedom can be minimized. Figure 5 shows the in-plane deformations and the out-of-plane rotations of the plate normals in the x' and y' directions. Note that this particular choice of the local coordinate system automatically eliminates the local out-of-plane deformations at each node (i.e., $w'_1 = w'_2 = w'_3 = 0$).

The element in-plane deformations u'_2, u'_3, and v'_3 can be calculated by comparing the deformed element to its undeformed state and by determining the amount it stretches (see Fig. 5).

Similarly, the element rotational deformations can be determined by comparing the deformed and undeformed unit vectors at the element nodes. The undeformed nodal vectors are normal to the plane formed by the triangle nodes at all times, and they coincide with the local z' axes. The deformed unit vectors are updated at each time step by the incremental rotations in the global x and y directions using the finite rotation relation

$$\boldsymbol{n}_d^{t^{n+1}} = \cos(\Delta\phi)\boldsymbol{n}_d^{t^n} + (1 - \cos(\Delta\phi))(\boldsymbol{n} \cdot \boldsymbol{n}_d^{t^n})\boldsymbol{n} + \sin(\Delta\phi)(\boldsymbol{n} \times \boldsymbol{n}_d^{t^n}) \tag{8a}$$

$$\Delta\phi = \sqrt{(\Delta\beta_x)^2 + (\Delta\beta_y)^2 + (\Delta\beta_z)^2} \tag{8b}$$

$$\boldsymbol{n} = (-\Delta\beta_y \boldsymbol{i} + \Delta\beta_x \boldsymbol{j} + \Delta\beta_z \boldsymbol{k})/\Delta\phi \tag{8c}$$

where $\Delta\phi$ is the magnitude of the rotation; $\boldsymbol{n}$ is the normalized rotation vector; and $\boldsymbol{n}_d^{t^n}$ and $\boldsymbol{n}_d^{t^{n+1}}$ are the deformed unit vectors at time steps t^n and t^{n+1}, respectively, expressed in the global coordinate system.

Although the incremental rotations at each step can be approximated as infinitesimal rotations, the use of finite rotation expressions was found to be more accurate, at a minimal increase in computational cost. By determining the amount of rotation that the undeformed vector must undergo to coincide with the corresponding deformed vector, local rotational deformations can be calculated in terms of the deformed unit vector $(\boldsymbol{n}_d^{t^n})^L$ expressed in local coordinates at the beginning of each time step t^n:

$$\beta_{x'} = (\boldsymbol{n}_d^{t^n})_x^L \frac{\cos^{-1}((\boldsymbol{n}_d^{t^n})_z^L)}{\sqrt{((\boldsymbol{n}_d^{t^n})_x^L)^2 + ((\boldsymbol{n}_d^{t^n})_y^L)^2}} \tag{9a}$$

$$\beta_{y'} = (\boldsymbol{n}_d^{t^n})_y^L \frac{\cos^{-1}((\boldsymbol{n}_d^{t^n})_z^L)}{\sqrt{((\boldsymbol{n}_d^{t^n})_x^L)^2 + ((\boldsymbol{n}_d^{t^n})_y^L)^2}} \tag{9b}$$

The approach is similar to a procedure described in [16].

B. Nonlinear Aerodynamic Model

The aerodynamic model used in the present study is based on a Galerkin finite element discretization of the classical Euler equations for a perfect gas, using the weak or integral form of the conservation laws:

$$\frac{\partial}{\partial t}\int_\Omega \boldsymbol{W}\,\mathrm{d}V + \int_{\partial\Omega} \boldsymbol{F}\cdot\boldsymbol{n}\,\mathrm{d}s = 0 \tag{10}$$

where Ω is an element volume with boundary $\partial\Omega$ moving with velocity $\boldsymbol{U}$, $\boldsymbol{n} = n_i\boldsymbol{e}_i$ is the outward unit normal to $\partial\Omega$, $\boldsymbol{e}_i$ are the unit vectors in the x_i directions, and

$$\boldsymbol{W} = \begin{bmatrix} \rho \\ \rho u_1 \\ \rho u_2 \\ \rho u_3 \\ \rho e \end{bmatrix}, \qquad \boldsymbol{F}_j = \begin{bmatrix} \rho(u_j - U_j) \\ \rho u_1(u_j - U_j) - \sigma_{1j} \\ \rho u_2(u_j - U_j) - \sigma_{2j} \\ \rho u_3(u_j - U_j) - \sigma_{3j} \\ \rho e(u_j - U_j) - \sigma_{ij}u_i \end{bmatrix} \tag{11}$$

where ρ is the density, $\boldsymbol{u}$ is the material velocity, e is the total energy per unit mass, σ_{ij} is the Cartesian stress tensor, and $\boldsymbol{F} = \boldsymbol{F}_j\boldsymbol{e}_j$. In the present inviscid (Euler) flow model, $\sigma_{ij} = -p\delta_{ij}$, and the equation of state can be used to eliminate the pressure:

$$p = \rho(\gamma - 1)[e - \tfrac{1}{2}u_i u_i] \tag{12}$$

The vector $\boldsymbol{W}$ of unknowns is approximated as

$$\boldsymbol{W}(x_1, x_2, x_3, t) = \sum_j \boldsymbol{W}_j(t)\varphi_j(x_1, x_2, x_3, t) \tag{13}$$

where $\boldsymbol{W}_j$ are the nodal values of $\boldsymbol{W}$, and φ_j are the linear shape functions. The finite element discretization is carried out by substituting Eq. (13) into the Galerkin form of Eq. (10) and applying the divergence theorem. The integrals are evaluated numerically using Gaussian integration, and the space-discretized nodal equations for the fluid domain become

$$\frac{\mathrm{d}}{\mathrm{d}t}\sum_j \boldsymbol{m}_{ij}\boldsymbol{W}_j + \boldsymbol{Q}_i - \boldsymbol{D}_i = 0 \tag{14}$$

where the summation on j extends over all nodes in the superelement, or control volume, associated with node i (i.e., the union of all elements that meet at node i); $\boldsymbol{m}_{ij}$ is the consistent mass matrix; $\boldsymbol{Q}_i$ is the flux vector; and the dissipative fluxes $\boldsymbol{D}_j$ are of the Jameson–Mavriplis type (see [17]).

A four-stage Runge–Kutta scheme is used to integrate the space-discretized system of nonlinear equations forward in time. To save computational time, the dissipative terms are evaluated only during the first two stages. Time accuracy is maintained by ensuring that the

fluid and structural finite element equations are time-marched simultaneously, within the same multistage Runge–Kutta execution loop. The numerical calculations start from the converged steady aeroelastic solution for the wing. A suitable initial velocity is then imparted to the model in bending or torsion, and the time marching is initiated.

C. Fluid–Structure Coupling

An important issue that must be addressed when coupling arbitrary CFD codes to finite element structural codes is the problem of compatibility or conformity at the fluid–structure boundary. Unless the required compatibility conditions are satisfied, coupling errors of unknown magnitude are introduced, which may seriously degrade the accuracy of the aeroelastic code [17]. In the direct Eulerian–Lagrangian scheme, both kinematic (tangent flow) and kinetic (force equilibrium) boundary conditions are imposed at the boundary.

The kinematic boundary condition of tangent flow can be stated in the form

$$\frac{\partial \boldsymbol{B}}{\partial t} + \boldsymbol{u} \cdot \nabla \boldsymbol{B} \equiv \frac{D\boldsymbol{B}}{Dt} = 0 \tag{15}$$

where $\boldsymbol{u}$ is the fluid velocity at the boundary and the preceding equation is satisfied at the instantaneous wing surface boundary, defined by $\boldsymbol{B}(x, y, z, t) = 0$. To describe the instantaneous locus of the wing surface accurately, an element-based approach compatible with the large-deformation formulation is used. The deformation of the wing surface is calculated using the values of the element nodal coordinates, and the displacement field is interpolated within each structural element using the corresponding FE shape functions. The corresponding surface velocity components at any point are obtained in a similar manner by using both the generalized displacements and the corresponding generalized velocities. Figures 6 and 7 illustrate this approach in 2-D and 3-D, respectively. Once the wing surface mesh nodes have been updated, a Jacobi iterative procedure based on a spring analogy is used to determine the locations of the remaining mesh nodes in the computational domain. Usually, three iterations suffice for acceptable convergence.

The spring analogy has certain limitations when used in problems involving moderate-to-large structural deformations, because of the tendency of certain mesh tetrahedra to suffer snap-through, resulting in a negative cell volume and a subsequent crash of the computational code. In the present study, the use of nonlinear springs was found to alleviate the problem somewhat, and wing tip deflections of the order of the wing chord can be accommodated in the time-marching flutter solution without encountering numerical difficulties.

The element-based approach is also employed in the consistent aerodynamic load calculations, as shown in Fig. 8. In this approach, force vectors are first calculated in the local element coordinate systems using 13-point Gaussian quadrature and then transformed to the global coordinate system for use in the time marching of the space-discretized aeroelastic equations. The aerodynamic loads are, in effect, modeled as follower forces, resulting in a more accurate prediction of the aeroelastic response.

Both the dynamic mesh motion and aerodynamic load calculations employ an initial mapping that establishes the relation between the

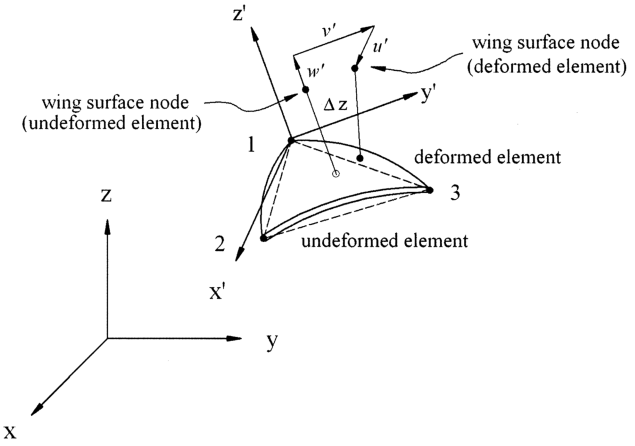

Fig. 7 Mesh motion kinematics in 3-D.

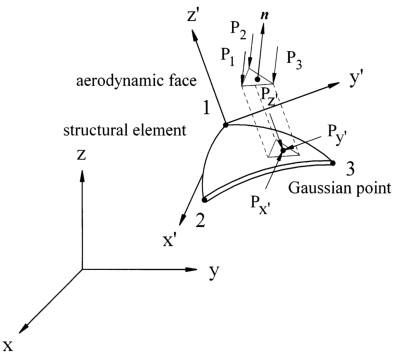

Fig. 8 Element-based consistent aerodynamic load calculations.

structural elements and aerodynamic faces on the wing surface. In this mapping, projections of the wing surface aerodynamic nodes on the corresponding structural elements provide the structural area coordinates A_i used in the dynamic mesh calculations. Similarly, projections of the Gaussian integration points onto the corresponding aerodynamic faces provide the corresponding area coordinates that are used in the pressure calculations. Figure 9 illustrates this mapping.

III. Results and Discussion

A. Nonlinear Structural Model Validation

The following examples show a few of the test cases studied during the validation of the structural model. As a first example, we consider the vertical and horizontal deflections of a cantilevered beam subjected to a static tip load (Fig. 10). This case was also studied in [18] using Bernoulli–Euler-beam finite elements and a midpoint tangent incremental solution scheme, combined with a coordinate transformation at each step. The results of the present calculations are based on a $2 \times 10 \times 2$ triangular-plate mesh, in which the beam is divided into 2 chordwise and 10 spanwise

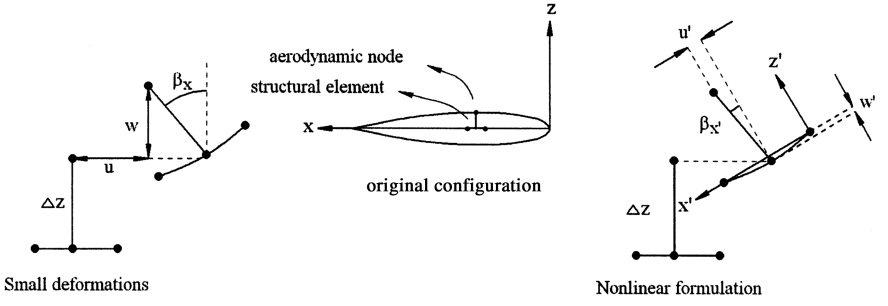

Fig. 6 Mesh motion kinematics in 2-D.

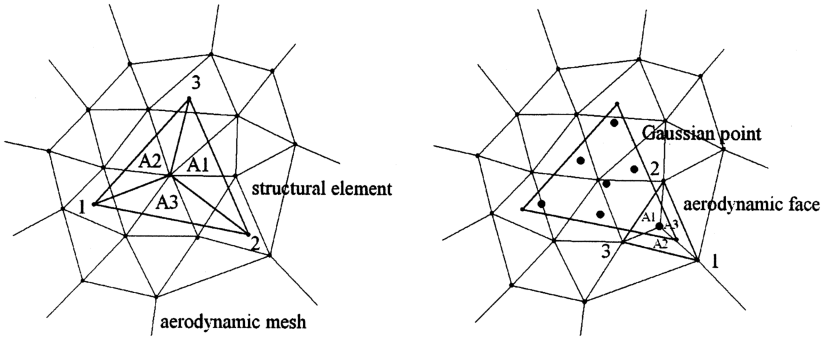

Fig. 9 Mapping of aerodynamic faces and structural elements.

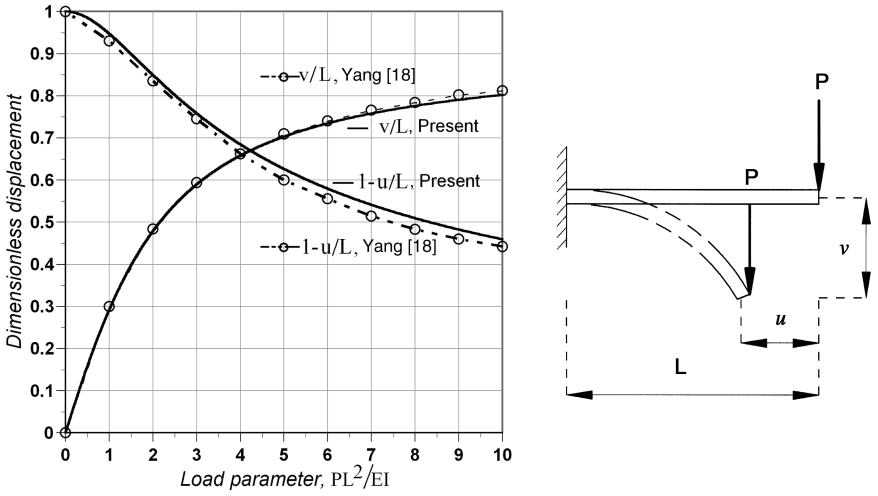

Fig. 10 Cantilevered beam with concentrated tip load.

rectangular segments, each divided into two triangles along one of the diagonals, resulting in 40 elements. The beam thickness h, width b, and length L are 0.1, 1, and 10 m, respectively, and a Poisson ratio of zero is assumed. The present results are in good agreement with those of [18], which in turn were shown to be in good agreement with the exact analytical beam solution in terms of elliptic integrals ([2] in [18]). Because the beam slenderness ratio in this example is $L/r = 346.4$, the effects of shear deformations should be small.

The second example is a cantilevered plate with a concentrated load acting on one of its corners, as shown in Fig. 11. Results obtained for this problem using 96 triangular elements ($6 \times 8 \times 2$ mesh) show good agreement with the results published in [16], with a 4% difference in the vertical corner deflection at the maximum load factor. It should be noted that shear deformation was not included in the finite element used in [16].

The final example considers the dynamic response of a cantilevered beam subjected to a uniformly distributed load (Fig. 12). A $2 \times 8 \times 2$ mesh (32 elements) was used in these calculations. Compared with the results published in [19], the present results show a nonlinear amplitude and period increase of approximately 9.5 and 3.7%, respectively. Five 8-node constant-stress elements were used in [19], using a Newmark integration scheme based on a total Lagrangian formulation. Because the rotational degrees of freedom and shear deformations were not included, a "stiffer" dynamic response is to be expected. Additional calculations using Euler beam elements (not shown) resulted in amplitude and period differences for the nonlinear response of approximately 2.9 and 2.7%, respectively, compared with the results in [19].

B. Nonlinear Flutter Calculations

The ONERA M6 wing model (Fig. 13) has been extensively studied in [4,11,17] using the linear DST structural model. Figure 14 compares the strong large-amplitude flutter behavior of this wing at $M = 0.84$, as predicted by the linear and nonlinear structural models for initial conditions corresponding to the first-bending-mode velocity distribution. The flutter mode is dominated by the first bending mode of the wing. Compared with the linear solution, there is roughly a 25% reduction in the flutter amplitude for the fourth flutter cycle and a reduction of about 40% in the growth of the total wing energy $E_{\text{tot}} = T + U$. This is mainly attributed to the nonlinear stiffening effects introduced by the nonlinear structural model. In these figures, W_e represents the work of the external (aerodynamic) forces. A check of the accuracy of the direct Eulerian–Lagrangian computations is provided by the difference $E_{\text{tot}} - W_e$, which should be a straight line in these calculations, because zero structural damping was assumed. This is seen to be the case in all calculations presented in this paper.

Figure 15 shows the nonlinear flutter behavior for initial velocity conditions corresponding to the first torsional mode of the wing. Strong flutter is again observed, and the dominant bending mode emerges after only one flutter cycle. As expected, the nonlinear structural model predicts a reduction in the flutter amplitude (35% for the fifth cycle) as well as in the wing total energy.

Figure 16 shows the neutrally stable ONERA M6 wing response, as predicted by the nonlinear structural model. The structural thickness ratio required for neutral stability is slightly higher than that predicted by the linear model (i.e., $h/c_r = 0.0255$ vs 0.250), whereas the flutter amplitudes are observed to be very close. Thus, from a structural design standpoint, the structural nonlinearities have a slightly *destabilizing* effect near the flutter boundary of the wing, despite the stiffening effects contributed by these nonlinearities.

Figure 17 shows the planform of the generic fighter wing studied in [9], which is a thin wing of relatively low aspect ratio (3.45) with a NACA 64006 airfoil section. Calculations based on the linear and nonlinear structural models are compared in Fig. 18. The nonlinear model results in a significant reduction in the flutter amplitude and energy growth rate. Calculations in [9] using a *damped* linear

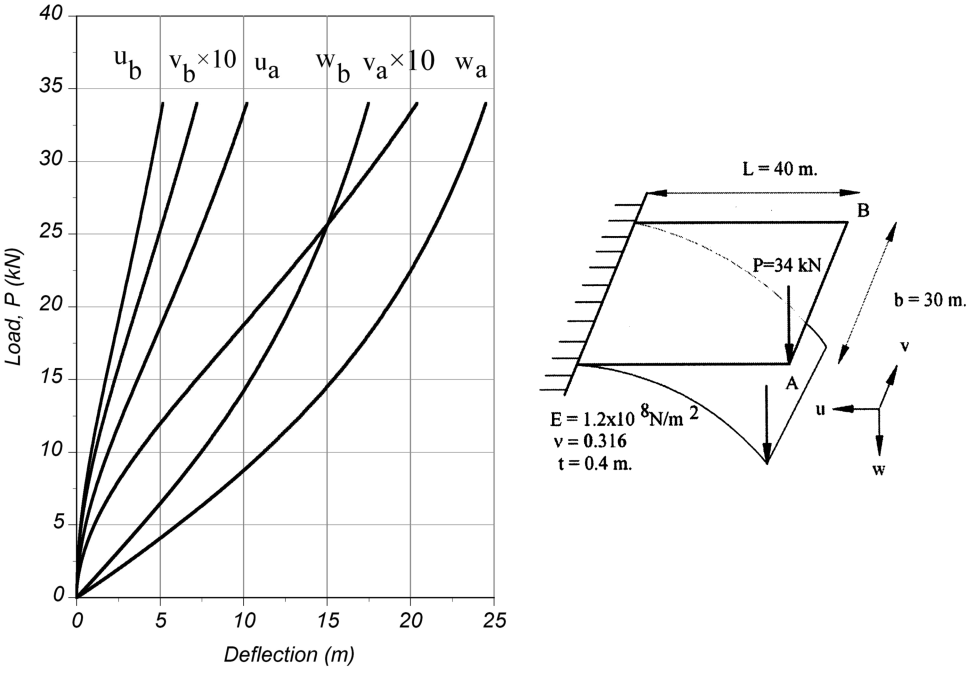

Fig. 11 Cantilevered plate with concentrated corner load.

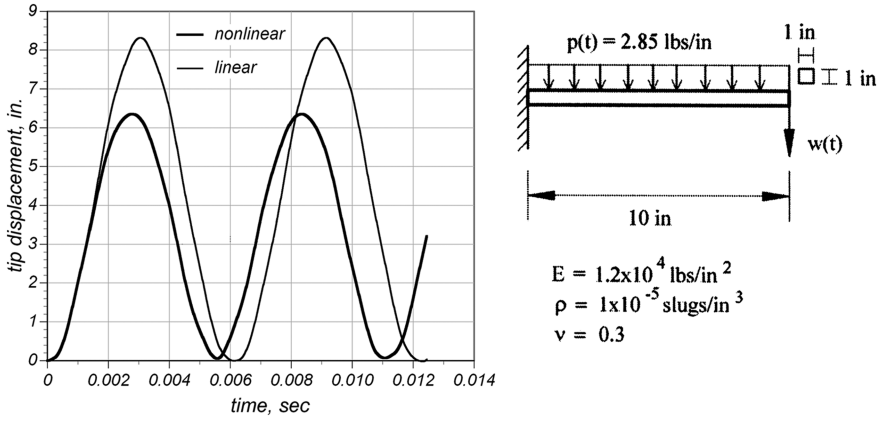

Fig. 12 Dynamic response of cantilevered beam with uniformly distributed load.

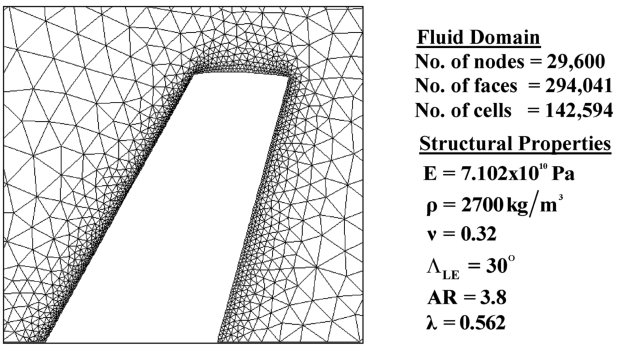

Fig. 13 The ONERA M6 wing.

structure revealed LCO-type flutter at this Mach number and angle of attack, even though the structural damping was relatively small ($g = 0.02$, or 1% of critical). In the present calculations with an undamped nonlinear structure with a plate thickness of $h/c_r = 0.012$, it is not clear if the solution is converging to a high-amplitude LCO, because the flutter amplitudes continue to grow until the code breaks down. However, if the wing structural plate thickness is increased slightly to $h/c_r = 0.0125$, limit-cycle flutter is observed (Fig. 19). These observations suggest that the addition of a small amount of structural damping to the nonlinear model with $h/c_r = 0.012$ would also result in limit-cycle flutter.

C. Comparisons with the von Kármán Finite Element Model

Figure 20 shows a comparison of the predictions of the von Kármán structural model with that of the present nonlinear finite element calculations for the case of a beam with a transverse load at the tip (Fig. 10). Figure 20a corresponds to the load parameter range in Fig. 10, in which the beam displacements are normalized with respect to the length of the beam L. Because the von Kármán model is valid only for displacement of the order of the plate (or beam) thickness or less, Fig. 20b shows the corresponding displacements normalized with respect to the beam thickness h for low values of the load parameter. As can be seen, the agreement between the von Kármán and the direct Eulerian–Lagrangian results is good up through transverse displacements v/h of about 2 (3.1% error), but the error rapidly increases as v/h increases beyond 4 (10.6% error), reaching 29.1% at $v/h = 10$. For large displacements of the order of the beam length, the von Kármán model yields results that are unacceptable even as a first approximation (see Fig. 20a).

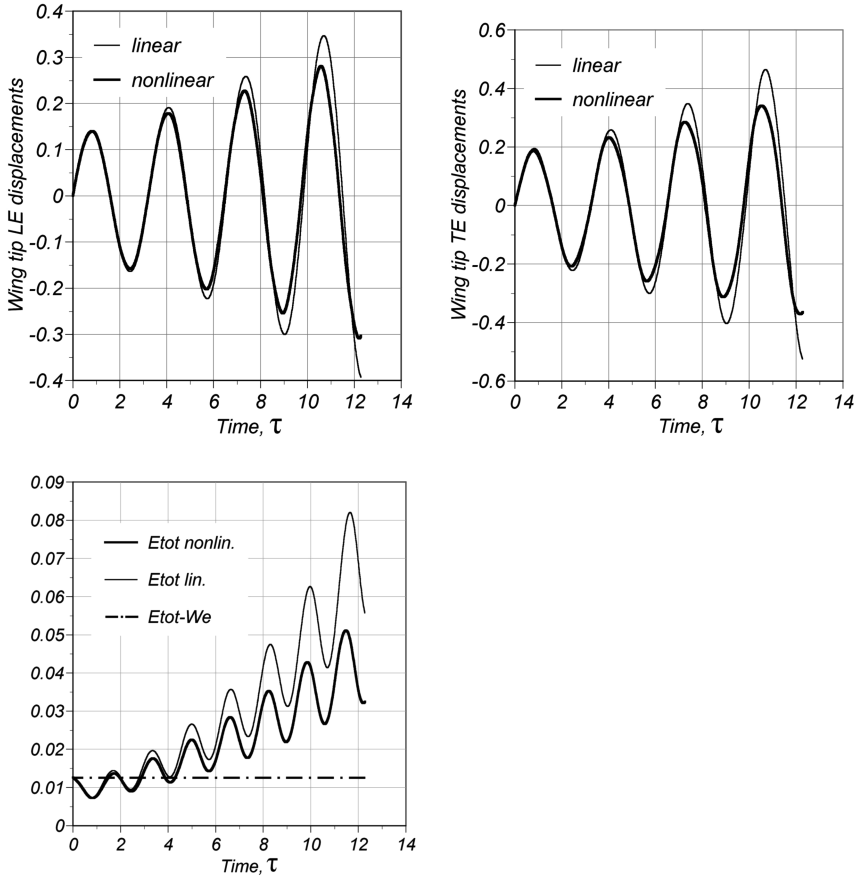

Fig. 14 Flutter response of the ONERA M6 wing with velocity initial conditions in the first bending mode ($h/c_r = 0.018$, $M = 0.84$, and $\alpha = 0\,\mathrm{deg}$) (henceforth, axes labels LE and TE denote the leading and trailing edge, respectively).

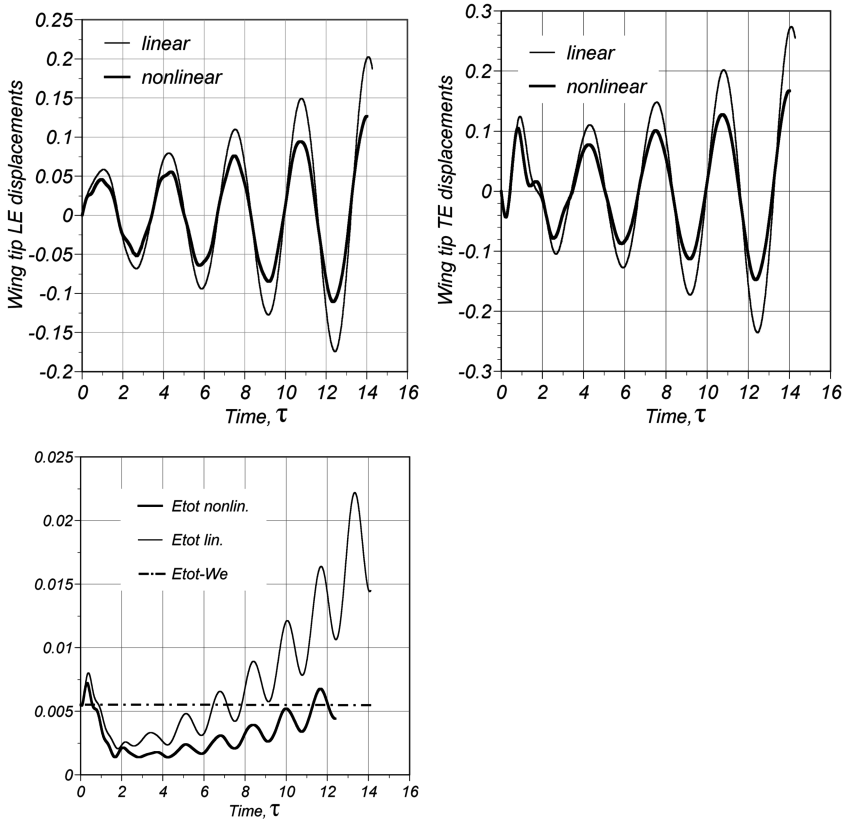

Fig. 15 Flutter response of the ONERA M6 wing with velocity initial conditions in the first torsion mode ($h/c_r = 0.018$, $M = 0.84$, and $\alpha = 0\,\mathrm{deg}$).

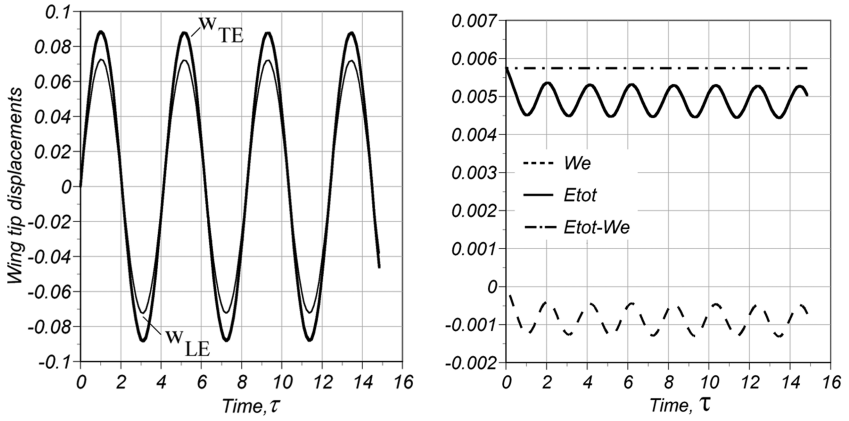

Fig. 16 Neutrally stable ONERA M6 wing with initial conditions in the first bending mode ($h/c_r = 0.0255$, $M = 0.84$, and $\alpha = 0$ deg).

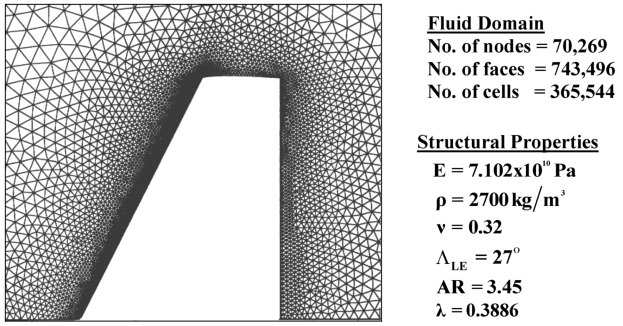

Fig. 17 The F-wing (generic fighter wing).

In the aeroelastic case, the differences between the von Kármán structural model and the present direct Eulerian–Lagrangian model are amplified because of the sensitivity of the flutter instability to wing deformations. Figure 21 shows a comparison of the calculated transonic flutter behavior of the ONERA M6 wing at Mach 0.84, using different structural models and initial conditions corresponding to 0.1 times the velocity distribution of the first natural bending mode of the wing. As can be seen, the calculation based on the von Kármán model greatly underestimates the growth of the wing total energy and thus completely misses the explosive nature of the emerging flutter. In fact, the linear structural model does a better job in this example, both qualitatively and quantitatively. Figure 22 shows a similar comparison for the same case, but with the initial condition increased by a factor of 10. Again, the von Kármán model predicts amplitude decay to a limit cycle, rather than rapidly growing flutter amplitudes.

IV. Conclusions

1) The nonlinear structural model based on the direct Eulerian–Lagrangian approach provides a computationally efficient foundation for nonlinear aeroelastic calculations using explicit multistage Runge–Kutta time-marching schemes.

2) Using element-level calculations in local Lagrangian reference frames, consistent aerodynamic load vectors of the "follower force" type can be obtained for cases involving both the effects of in-plane and out-of-plane motions of the wing.

3) In the case of the ONERA M6 wing, the structural nonlinearities have a slightly destabilizing effect near the flutter boundary at Mach 0.84, despite the stiffening effects contributed by these nonlinearities.

4) The classical nonlinear von Kármán plate theory performs well only for problems with deformations of the order of the plate thickness. In the case of a cantilever beam with a tip load, for example, the error in the predicted transverse displacement v is 3% for $v/h = 2$, but increases rapidly as v/h increases beyond 4 (10.6% error), reaching 29.1% when $v/h = 10$.

5) In nonlinear aeroelastic analysis of wings for which moderate-to-large translations and rotations occur, the von Kármán plate theory greatly overestimates the nonlinear stiffening arising from the

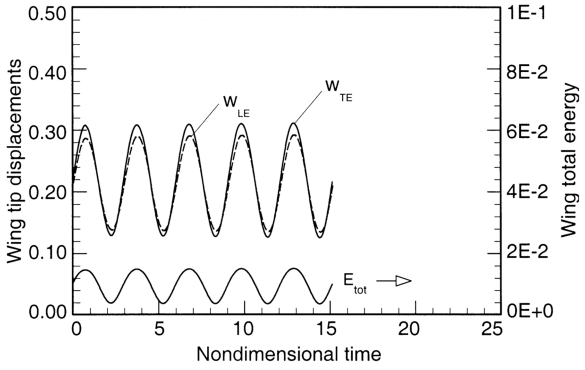

Fig. 19 Transonic limit-cycle flutter of the F-wing ($h/c_r = 0.0125$, $M = 0.90$, and $\alpha = 3.0$ deg).

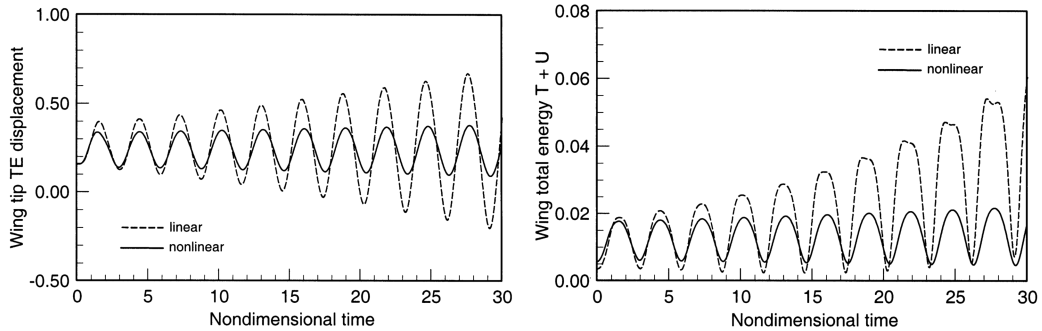

Fig. 18 Comparison of calculated transonic flutter response of the F-wing as predicted using the linear vs the nonlinear structural model with velocity initial conditions in the first bending mode ($h/c_r = 0.012$, $M = 0.90$, and $\alpha = 3.0$ deg).

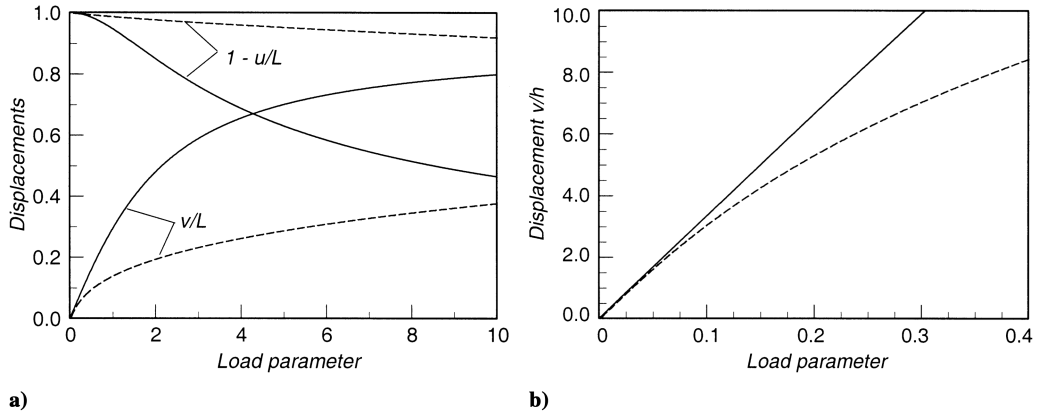

Fig. 20 Comparison of displacement predictions for a cantilever beam with tip load; direct Eulerian–Lagrangian FEM (solid lines) and von Kármán FEM (dashed lines).

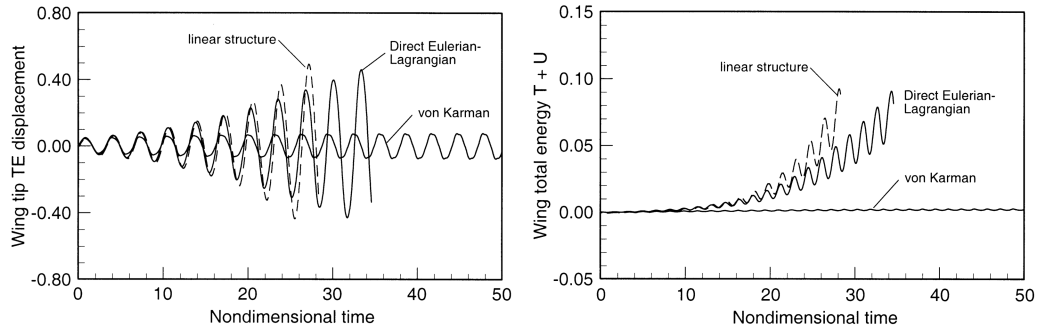

Fig. 21 Comparison of calculated transonic flutter behavior of the ONERA M6 wing using different structural models with small-velocity initial conditions in the first bending mode ($h/c_r = 0.018$ and $M = 0.84$).

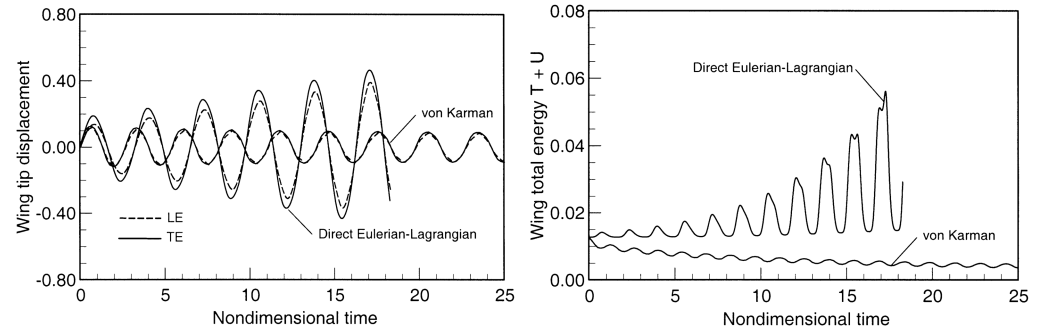

Fig. 22 Comparison of calculated transonic flutter behavior of the ONERA M6 wing using different structural models with large-velocity initial conditions in first bending mode ($h/c_r = 0.018$ and $M = 0.84$).

coupling between the in-plane and out-of-plane deformations, resulting in large errors in the predicted flutter amplitudes. In some cases, small-amplitude limit-cycle flutter is predicted, whereas the present nonlinear aeroelastic code predicts explosive flutter.

Acknowledgment

This research was supported by NASA grants NCC 2-234, NCC 4-153, and NCC 4-157.

References

[1] Kousen, K. A., and Bendiksen, O. O., "Nonlinear Aspects of the Transonic Aeroelastic Stability Problem," 29th AIAA/ASME/AHS/ASCE Structures, Structural Dynamics, and Materials Conference, AIAA, Reston, VA, 18–20 Apr. 1988, pp. 760–769.

[2] Kousen, K. A., and Bendiksen, O. O., "Limit Cycle Phenomena in Computational Transonic Aeroelasticity," *Journal of Aircraft*, Vol. 31, Nov.–Dec. 1994, pp. 1257–1263.

[3] Davis, G. A., and Bendiksen, O. O., "Transonic Panel Flutter," AIAA Paper 93-1476, Apr. 1993.

[4] Bendiksen, O. O., and Hwang, G., "Nonlinear Flutter Calculations for Transonic Wings," *CEAS International Forum on Aeroelasticity and Structural Dynamics*, Vol. 2, Esagrafica, Rome, 17–20 June 1997, pp. 105–114.

[5] Gordnier, R. E., "Computation of Limit Cycle Oscillations of a Delta Wing," 43rd AIAA/ASME/ASCE/AHS/ASCE Structures, Structural Dynamics, and Materials Conference, Denver, CO, AIAA Paper 2002-1411, Apr. 2002.

[6] Pranata, B. B., Kok, J. C., Spekreijse, S. P., Hounjet, M. H. L., and Meijer, J. J., "Simulation of Limit Cycle Oscillation of Fighter Aircraft at Moderate Angle of Attack," *Proceedings of the International Forum on Structural Dynamics and Aeroelasticity 2003* [CD-ROM], Netherlands Association of Aeronautical Engineers, Amsterdam, The Netherlands, 4–6 June 2003.

[7] Attar, P. J., Dowell, E. H., and White, J. R., "Modeling the LCO of a Delta Wing Using a High Fidelity Structural Model,", 45th AIAA/ASME/ASCE/AHS/ASCE Structures, Structural Dynamics, and Materials Conference, Palm Springs, CA, AIAA Paper 2004-1692, Apr. 2004.

[8] Thomas, J. P., Dowell, E. H., and Hall, K. C., "Modeling Limit Cycle Oscillation Behavior of the F-16 Fighter Using a Harmonic Balance Approach," 45th AIAA/ASME/ASCE/AHS/ASCE Structures, Structural Dynamics, and Materials Conference, Palm Springs, CA, AIAA Paper 2004-1696, Apr. 2004.

[9] Bendiksen, O. O., "Transonic Limit Cycle Flutter/LCO," 45th AIAA/ASME/ASCE/AHS/ASCE Structures, Structural Dynamics, and Materials Conference, Palm Springs, CA, AIAA Paper 2004-1694, Apr. 2004.

[10] Bendiksen, O. O., "A New Approach to Computational Aeroelasticity," 32nd AIAA/ASME/AHS/ASCE Structures, Structural Dynamics, and Materials Conference, AIAA, Reston, VA, 8–10 Apr. 1991, pp. 1712–1727.

[11] Hwang, G., "Parallel Finite Element Solutions of Nonlinear Aeroelastic and Aeroservoelastic Problems in Three-Dimensional Transonic Flows," Ph.D. Dissertation, Mechanical and Aerospace Engineering Dept., Univ. of California, Los Angeles, Mar. 1997.

[12] Batoz, J. L., and Lardeur, P., "A Discrete Shear Triangular Nine D.O.F. Element for Analysis of Thick to Very Thin Plates," *International Journal for Numerical Methods in Engineering*, Vol. 28, No. 3, 1989, pp. 533–560.
doi:10.1002/nme.1620280305

[13] Patel, S., "A Discrete Shear Triangular Finite Element with Applications to the Vibration Analysis of Thin and Thick Plates," M.S. Thesis, Dept. of Mechanical and Aerospace Engineering, Univ. of California, Los Angeles, 1995.

[14] Rajasekaran, S., and Murray, D. W., "Incremental Finite Element Matrices," *Journal of the Structural Division*, Vol. 99, No. 12, Dec. 1973, pp. 2423–2438.

[15] Seber, G., "Aeroelastic Wing Response Analysis Using Finite Elements in a Large Deformation Direct Eulerian–Lagrangian Formulation," Ph.D. Dissertation, Mechanical and Aerospace Engineering Dept., Univ. of California, Los Angeles, June 2004.

[16] Hsiao, K., "Nonlinear Analysis of General Shell Structural by Flat Triangular Shell Element," *Computers and Structures*, Vol. 25, No. 5, 1987, pp. 665–675.
doi:10.1016/0045-7949(87)90159-3

[17] Bendiksen, O. O., "Modern Developments in Computational Aeroelasticity," *Proceedings of the Institution of Mechanical Engineers, Part G (Journal of Aerospace Engineering)*, Vol. 218, No. 3, June 2004, pp. 157–177.
doi:10.1243/0954410041872861

[18] Yang, T. Y., "Matrix Displacement Solution to Elastica Problems of Beams and Frames," *International Journal of Solids and Structures*, Vol. 9, No. 7, 1973, pp. 829–842.
doi:10.1016/0020-7683(73)90006-1

[19] Bathe, K. J., Ramm, E., and Wilson, E. L., "Finite Element Formulations for Large Deformation Dynamic Analysis," *International Journal for Numerical Methods in Engineering*, Vol. 9, No. 2, 1975, pp. 353–386.
doi:10.1002/nme.1620090207

C. Cesnik
Associate Editor